






Field-induced spin reorientation transitions in antiferromagnetic ring-shaped spin chainsYelyzaveta A. Borysenko ^{1,2,3} Denis D. Sheka ¹ Jürgen Fassbender ² Jeroen van den Brink,^{3,4}
Denys Makarov ² and Oleksandr V. Pylypovskyi ^{2,5,*}¹*Taras Shevchenko National University of Kyiv, 01601 Kyiv, Ukraine*²*Helmholtz-Zentrum Dresden-Rossendorf e.V., Institute of Ion Beam Physics and Materials Research, 01328 Dresden, Germany*³*Institute for Theoretical Solid State Physics, Leibniz IFW Dresden, 01069 Dresden, Germany*⁴*Institute for Theoretical Physics and Würzburg-Dresden Cluster of Excellence ct.qmat,
Technische Universität Dresden, 01069 Dresden, Germany*⁵*Kyiv Academic University, 03142 Kyiv, Ukraine*

(Received 5 August 2022; revised 9 October 2022; accepted 9 November 2022; published 21 November 2022)

Easy axis antiferromagnets are robust against external magnetic fields of moderate strength. Spin reorientations in strong fields can provide insight into more subtle properties of antiferromagnetic materials, which are often hidden by their high ground-state symmetry. Here, we investigate theoretically effects of curvature in ring-shaped antiferromagnetic achiral anisotropic spin chains in strong magnetic fields. We identify the geometry-governed helimagnetic phase transition above the spin-flop field between vortex and onion states. The curvature-induced Dzyaloshinskii–Moriya interaction results in the spin-flop transition being of first or second order, depending on the ring curvature. Spatial inhomogeneity of the Néel vector in the spin-flop phase generates weak ferromagnetic response in the plane perpendicular to the applied magnetic field. Our paper contributes to the understanding of the physics of curvilinear antiferromagnets in magnetic fields and guides prospective experimental studies of geometrical effects relying on spin-chain-based nanomagnets.

DOI: [10.1103/PhysRevB.106.174426](https://doi.org/10.1103/PhysRevB.106.174426)**I. INTRODUCTION**

Antiferromagnets (AFMs) represent a broad class of multilattice magnetic materials, whose magnetic symmetry group contains an element of sublattice permutation [1–3]. In addition to their application potential for high-speed and low-power magnetic memory and logic devices [3–5], AFMs are complex nonlinear systems, which makes them appealing for fundamental research. This includes studies of material properties considering crystal symmetries [6], magnetization dynamics, and topological solitons [7,8]. Being robust against moderate magnetic fields, AFMs possess a family of spin-flop transitions characterized by the reorientation of the Néel order parameter in sufficiently strong fields. The spin-flop phase is a characteristic property of the given AFM, in which the energetically preferable orientation of the primary order parameter is perpendicular to the easy axis of anisotropy [7,9]. Transition to the spin-flop phase reveals the presence of additional anisotropy axes [10,11] and can support magnetic solitons [7,8,12]. In the vicinity of or as a consequence of the phase transition, magnetic responses of AFMs can be modified. Indeed, entering the spin-flop phase reduces the potential barrier for magnetoelectric switching [13], enables long-distance spin transport [14], enhances the skyrmion lifetime [15], and strengthens the magnetoelectric coupling [16]. These effects have been intensively studied for bulk AFMs, extended two-dimensional systems, and straight spin chains [2].

In particular, in the case of a straight anisotropic 1D wire with easy axis anisotropy, the spin flop is the first-order transition between different uniform states. Furthermore, there are studies which address quantum effects and cover the influence of sample boundaries and defects on the spin-flop transition [17,18].

The geometry of a magnetic sample provides an additional degree of freedom to tune its anisotropic and chiral responses [19–22]. Geometrical bends and twists in intrinsically achiral antiferromagnetic spin chains enable helimagnetic responses in the ground states [23]. Geometry-governed modifications of the linear spin dynamics suggest a possibility to form Bose–Einstein condensates for magnons in k space in helix-shaped chains [23] and allow tuning the propagation direction of spin waves of different polarizations [24]. Being highly sensitive to boundary conditions, AFMs support a variety of noncollinear spin textures in the ring geometry, including the Möbius state [25]. AFM domain walls [26] and skyrmions [27] in curvilinear antiferromagnetic thin films are affected by curvature gradients. Beyond the effects predicted for curvilinear antiferromagnets within the σ -model [23,26], curvilinear AFM spin chains bring about the geometry-governed weak ferromagnetism [28]. However, spin reorientation transitions in curvilinear AFMs exposed to strong magnetic fields remain unexplored.

Here, we investigate field-induced spin reorientation transitions in curvilinear ring-shaped intrinsically achiral anisotropic antiferromagnetic spin chains with even number of spins. This includes the highly symmetric case of the field applied along the ring axis and a finite angle between this

*o.pylypovskyi@hzdr.de

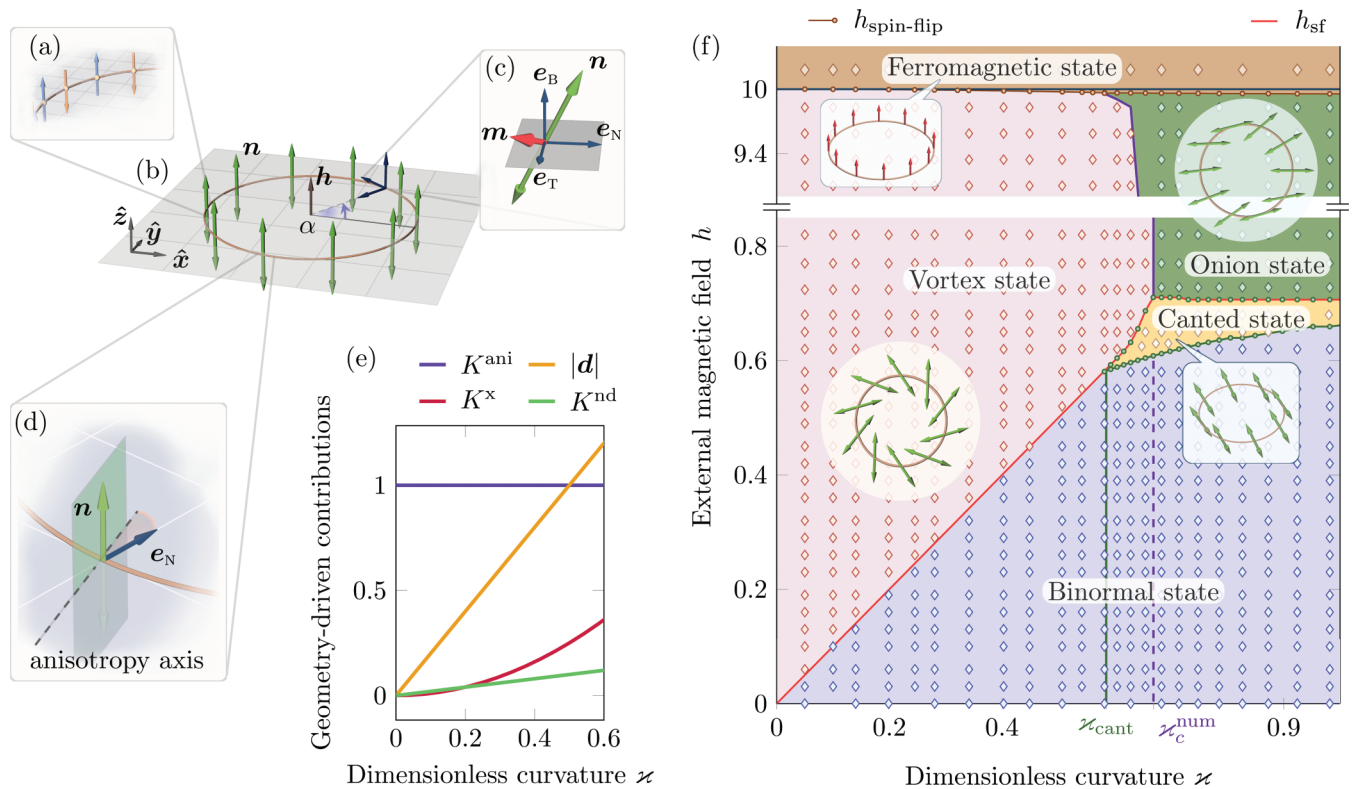


FIG. 1. Antiferromagnetic (AFM) spin chain shaped as a ring exposed to an external magnetic field applied perpendicular to the ring plane. (a) Schematics of the discrete model with arrows of blue and orange colors corresponding to the two AFM sublattices. (b) AFM ring in the ground (binormal) state. Double green arrow represents the orientation of the Néel vector \mathbf{n} . Azimuthal angle α measures coordinate along the ring. (c) TNB and local magnetic reference frames. (d) Tilt of the anisotropy axes. The green plane indicates the easy plane for the Néel vector. (e) Relation between the geometry-governed anisotropic (K^{ani} , K^x , K^{nd}) and chiral (d) contributions in the energy functional. (f) Equilibrium magnetic textures in field h applied perpendicular to the ring plane. Symbols represent the data obtained from spin-lattice simulations. Solid black line corresponds to the spin-flip field $h^s = 1/\epsilon$ and red line is the spin-flop field.

axis and magnetic field. Using the methodology of curvilinear magnetism, we show that the spin-flop state in a ring geometry enables a helimagnetic transition between the locally homogeneous (vortex) and periodic (onion) AFM textures, which is controlled by the ring curvature. The spin-flop transition for a large enough curvature is supplemented by an intermediate canted state, which we associate with the curvature-induced exchange-driven Dzyaloshinskii–Moriya interaction (DMI). The description of the curvature-induced weak ferromagnetic response in the spin-flop phase is provided as well.

The paper is organized as follows. In Sec. II, the model of ring-shaped AFM spin chains is introduced. In Sec. III, spin-flop phases in the magnetic field applied along the ring axis (the most symmetric case) are discussed. The behavior of the spin chain in the field applied under an angle to the ring axis is considered in Sec. IV. Estimations of the characteristic parameters for real nanomagnets are provided in Sec. V. In the Appendices, we summarize further details of spin-lattice simulations (Appendix A), offer information on the transition between the discrete and continuum model (Appendix B), and describe the spin-flop vortex phase (Appendix C).

II. THE MODEL

We consider an intrinsically achiral ring-shaped spin chain with an even number of magnetic moments N and the

nearest-neighbor AFM exchange integral \mathcal{J} . This leads to the appearance of two ferromagnetically ordered sublattices with opposite directions of magnetic moments, see Fig. 1(a). The lattice can be considered as a set of dimers with antiparallel orientation of spins in each dimer. The latter allows us to use an alternative representation of the magnetic ordering in terms of the reduced Néel vector $\mathbf{n}(\mathbf{r})$ and reduced magnetization vector $\mathbf{m}(\mathbf{r})$ (with \mathbf{r} being the radius vector) introduced as the difference and sum of magnetic moments of each AFM dimer along the chain, respectively [Fig. 1(b)]. These order parameters can be introduced for a 1D AFM system in such a way to obey the relations $\mathbf{n} \cdot \mathbf{m} = 0$ and $\mathbf{n}^2 + \mathbf{m}^2 = 1$. In the following, we limit our discussion to the case of the single-ion anisotropy with the hard axis of anisotropy along the tangential direction to the ring and spin-lattice coefficient \mathcal{K} . The sample's geometry is characterized by the curvature $\kappa = 2\pi/(Na_0)$ with a_0 being the distance between the neighboring magnetic moments, represented by spins of length S . The local reference frame (referred to as the TNB frame) consists of the tangential \mathbf{e}_T , normal \mathbf{e}_N and binormal \mathbf{e}_B vectors, see Figs. 1(b) and 1(c). The azimuthal angle α , which measures the coordinate along the ring, is counted counterclockwise starting from the x axis [Fig. 1(b)].

Micromagnetic description of a spin lattice in terms of continuous functions $\mathbf{n}(\mathbf{r})$ and $\mathbf{m}(\mathbf{r})$ is possible if the spatial variation of the order parameter is much larger than the

characteristic length scale represented by a magnetic length $\ell = a_0\sqrt{|\mathcal{J}/\mathcal{K}|} \gg a_0$, which determines the competition between the exchange and anisotropy energies. In this case, the magnetic energy of the ring reads

$$E/E_0 = \int (\mathcal{E}_x + \mathcal{E}_{\text{an}} + \mathcal{E}_f) d\alpha, \quad (1)$$

with $E_0 = \mathcal{K}S^2/(2a_0)$, see Appendix A for the respective spin-lattice Hamiltonian and details of simulations. The exchange energy density $\mathcal{E}_x = \mathbf{m}^2/\zeta^2 + 2(\mathbf{n}^2 - \mathbf{m}^2) + 2\mathbf{n}' \cdot \mathbf{m}/\zeta$ includes the uniform exchange assuring the absence of magnetization in equilibrium, the inhomogeneous exchange responsible for the stabilization of the uniform ground state without external fields, and the lifting term specific for 1D antiferromagnets and responsible for the appearance of the finite magnetization at noncollinear textures [28,29]. The prime denotes the spatial derivative $\mathbf{n}' = \varkappa\partial_\alpha\mathbf{n}$ with $\varkappa = \kappa\ell$ being the dimensionless curvature. The so-called expansion coefficient $\zeta = a_0/(2\ell) = \sqrt{|\mathcal{K}/(4\mathcal{J})|}$ characterizes the relation between the effective exchange and anisotropy fields. Associating the Néel vector with the first magnetic moment in each dimer, the intrinsic anisotropy reads $\mathcal{E}_{\text{an}} = K^{\text{ani}}n_{\text{T}}^2 + K^{\text{nd}}n_{\text{T}}n_{\text{N}}$, where $K^{\text{ani}} = 1$ for the dimensionless energy density and $K^{\text{nd}} = 2\zeta\varkappa$ [28]. Here, the hard axis $\mathbf{e}_{\text{ani}} = \mathbf{e}_{\text{T}}$ is taken into account. The second term in \mathcal{E}_{an} , with K^{nd} being the coefficient of nondiagonal components of the effective anisotropy matrix, reflects the numbering of moments (see Appendix B) and the variation of the anisotropy axis within each AFM dimer. The last term in energy Eq. (1), $\mathcal{E}_f = -(2/\zeta)\mathbf{m} \cdot \mathbf{h}$, represents the interaction of magnetic moments with the normalized external magnetic field $\mathbf{h} = \mathbf{H}/H_0$, where the characteristic field $H_0 = (S/\mu_{\text{B}})\sqrt{|\mathcal{J}/\mathcal{K}|}$ and μ_{B} is the Bohr magneton.

Within the σ -model (case of $m \ll 1$), the expression for the exchange energy density simplifies to $\mathcal{E}_x = \mathbf{n}^2 = \sum_{i=\text{T,N,B}} n_i^2 + \mathcal{E}_x^{\text{an}} + \mathcal{E}_x^{\text{DM}}$ [23,28]. Here, $\mathcal{E}_x^{\text{an}} = -K^x n_{\text{B}}^2$ with $K^x = \varkappa^2$ is the curvature-induced anisotropy stemming from exchange. Using the Einstein summation rule, the last term reads $\mathcal{E}_x^{\text{DM}} = \epsilon_{ijk}d_i n_j n'_k$, with ϵ_{ijk} being the Levi-Civita symbol and $\mathbf{d} = 2\varkappa\mathbf{e}_{\text{B}}$ by its symmetry represents the curvature-induced DMI for components of \mathbf{n} in the curvilinear reference frame [23]. This expression for \mathbf{n}^2 can be used in a general case as well.

The field-driven reorientation phase transitions are primarily determined by the anisotropic properties of the sample. For example, at the micromagnetic level, the dipolar interaction leads to the same hard-tangential anisotropy as the one introduced above. The strength of this anisotropy is independent of the geometry. For convenience, we normalize each energy term in Eq. (1) to this anisotropy, see purple line in Fig. 1(e) ($K^{\text{ani}} = 1$). The exchange energy in curvilinear AFM spin chains provides the chiral DMI-like response, whose strength is characterized by \varkappa [orange line in Fig. 1(e)], and the anisotropic response, which scales as \varkappa^2 and induces the easy axis along \mathbf{e}_{B} , see red line (K^x) in Fig. 1(e). The geometry-governed anisotropic contribution with the coefficient K^{nd} provides a tilt of the in-plane anisotropy axes, see green line in Fig. 1(e) and schematics in Fig. 1(d).

III. REORIENTATION PHASE TRANSITIONS IN MAGNETIC FIELD APPLIED ALONG THE RING AXIS

Figure 1(f) shows spin reorientation phase transitions in AFM rings of different curvatures \varkappa exposed to an external magnetic field \mathbf{h} applied along \mathbf{e}_{B} (perpendicular to the ring plane). The diagram includes five different phases. The easy axis of anisotropy stemming from exchange enables the spin-flop transition at field h_{sf} . Below h_{sf} , there is the only ground state with \mathbf{n} oriented along \mathbf{e}_{B} [binormal state, blue region in Fig. 1(f)] [23]. Fields stronger than h_{sf} induce the reorientation of \mathbf{n} and develop a static finite magnetic moment of the ring

$$\mathbf{m} = \zeta\mathbf{n} \times [(\mathbf{h} - \mathbf{n}') \times \mathbf{n}] + \mathcal{O}(\zeta^2) \quad (2)$$

for $h \gtrsim h_{\text{sf}}$, where the term \mathbf{n}' is responsible for the geometry-governed weak ferromagnetism [28]. We find that the field configuration $\mathbf{h} \parallel \mathbf{e}_{\text{B}}$ supports two equilibrium states in the spin-flop phase, depending on the ring radius. If the sample is sufficiently large (i.e., curvature is less than the critical one discussed below, $\varkappa < \varkappa_c$), the vortex state appears for $h > h_{\text{sf}} = \varkappa$ [pink shaded region in Fig. 1(f)], see details in Ref. [28]. In rings with curvature larger than \varkappa_c , there appears a magnetic texture of other symmetry, which is referred to as the onion state [green shaded region in Fig. 1(f)]. In each ground state in the spin-flop phase, the distribution of the Néel vector lies in the ring plane. In strong enough fields, the sample becomes completely saturated experiencing the spin-flip transition [brown shaded region in Fig. 1(f)].

In the vicinity of the spin-flop phase transition, the magnetization Eq. (2) is small [30]. In this case, the magnetic energy of the ring reads

$$E = E_0 \int \mathcal{E} d\alpha, \quad \mathcal{E} = \mathbf{n}^2 + n_{\text{T}}^2 + K^{\text{nd}}n_{\text{T}}n_{\text{N}} - h^2 + \mathcal{O}(\zeta^2). \quad (3)$$

To find the equilibrium distributions of the order parameters, we parametrize the Néel vector as $\mathbf{n} = \mathbf{e}_{\text{T}} \sin \vartheta \cos \varphi + \mathbf{e}_{\text{N}} \sin \vartheta \sin \varphi + \mathbf{e}_{\text{B}} \cos \vartheta$ with ϑ and φ being the polar and azimuthal angles in the local spherical reference frame. In the spin-flop phase, \mathbf{n} lies in the ring plane corresponding to $\vartheta = \pi/2$. The spatial distribution of \mathbf{n} is described by $\varphi(\alpha)$. As a consequence of the curvature-induced tilt of the anisotropy axes from the TNB directions, it is convenient to describe the $\mathbf{n}(\alpha)$ distribution by measuring the dependence of the angle between \mathbf{n} and the in-plane anisotropy axis, $\Phi(\alpha) = \varphi(\alpha) - (1/2)\arctan 2\zeta\varkappa$. Minimization of energy (3) with respect to Φ gives the following equation:

$$\varkappa^2 \partial_{\alpha\alpha} \Phi + \sin \Phi \cos \Phi = 0. \quad (4)$$

The vortex state solution with spatially homogeneous distributions of \mathbf{m} and \mathbf{n} in the local reference frame is stable for the case of small curvatures. This corresponds to $\Phi = \pi/2$ [28] and the energy of the vortex state reads $E_{\text{vor}}/E_0 = 2\pi(\varkappa^2 - h^2) + \mathcal{O}(\zeta^2)$. A spatially inhomogeneous solution of (4), $\Phi = -\text{am}(x, k)$, with $x = \frac{2K(k)}{\pi}\alpha$ which is characterized by the following distribution:

$$\mathbf{n} = \mathbf{e}_{\text{T}}\text{cn}(x, k) - \mathbf{e}_{\text{N}}\text{sn}(x, k) + \mathcal{O}(\zeta), \quad (5)$$

where $\text{cn}(\bullet, k)$ and $\text{sn}(\bullet, k)$ are the elliptic cosine and sine with modulus k , respectively [31], see Figs. 2(a) and 2(b). In line with states exhibiting similar symmetry in ferromagnetic

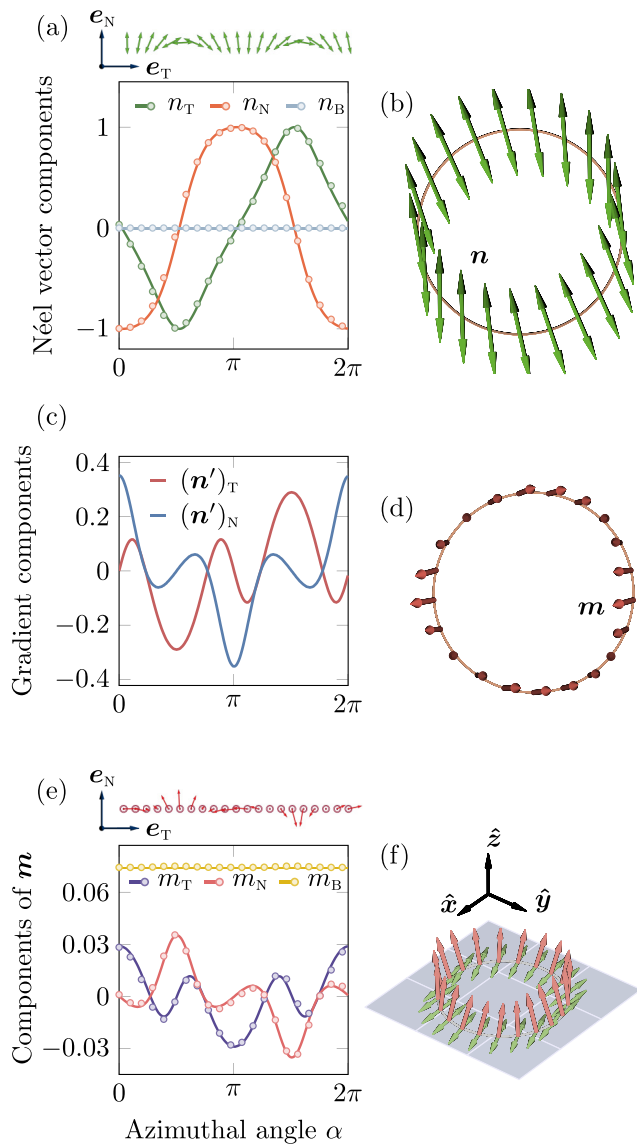


FIG. 2. Onion state in the ring with curvature $\varkappa = 0.75$ exposed to the magnetic field $\mathbf{h} = 0.74\mathbf{e}_B$. (a) Components of the Néel vector \mathbf{n} . (b) Schematics of the Néel vector \mathbf{n} for the onion texture. (c) Gradient components of \mathbf{n} . (d) Schematics of the magnetization vector \mathbf{m} for the onion texture. (e) Components of the magnetization vector \mathbf{m} . (f) Superimposed Néel and magnetization vectors (not to scale). In panels (a) and (e), symbols represent data obtained from spin-lattice simulations, solid lines correspond to Eqs. (5) and (7).

rings [32–34] and spherical shells [35,36], we refer to the distribution Eq. (5) as the onion state. In this expression, it is taken into account that opposite directions of \mathbf{n} are physically equivalent. The ring geometry imposes the boundary condition on Φ , from which the value of k for the given curvature is determined,

$$2\varkappa kK(k) = \pi, \quad (6)$$

where $K(k)$ is the complete elliptic integral of the first kind [31]. This gives the energy of the onion texture to be equal to $E_{\text{on}}/E_0 = 8\varkappa E(k)/k + 2\pi(1 - 1/k^2 - \varkappa^2 - h^2) +$

$\mathcal{O}(\varepsilon)$, with $E(k)$ being the complete elliptic integral of the second kind [31]. The critical curvature $\varkappa_c \approx 0.657$ separates the vortex and onion states. Its value is the solution of the equation $E_{\text{vor}}(\varkappa) = E_{\text{on}}(\varkappa)$. The boundary between these states in simulations is $\varkappa_c^{\text{num}} = 0.669 \pm 0.014$ and remains constant up to strong fields of $h \sim 7$. We note that for ferromagnetic rings in the absence of the external magnetic field, a similar geometrical phase transition between textures of different symmetries is observed with the critical curvature close to \varkappa_c [34].

The presence of large spatial derivatives of the components of the Néel vector [Fig. 2(c)] along the tangential direction in the onion state is reflected in the appearance of the local magnetization. Substituting the expression Eq. (5) in Eq. (2), the local direction of the magnetization vector reads

$$\mathbf{m} = \pm \zeta \left[\frac{1}{k} \text{dn}(x, k) - \varkappa \right] [\mathbf{e}_T \text{sn}(x, k) + \mathbf{e}_N \text{cn}(x, k)] + \mathbf{e}_B \zeta h + \mathcal{O}(\zeta^2), \quad (7)$$

where $\text{dn}(\bullet, k)$ is the delta amplitude [31], see Figs. 2(d) and 2(e). In contrast to the spin-flop vortex state with the locally homogeneous magnetization [28], the local magnetic moment of the onion state is nonuniform and depends on \varkappa , cf. Figs. 2(c) and 2(e). The binormal component of \mathbf{m} is determined by \mathbf{h} . The tangential and normal projections of \mathbf{m} are even and odd functions of α , respectively. We note that the energy is degenerate with respect to the sign change of \mathbf{n} as well as the in-plane components of \mathbf{m} . Schematics of both order parameters in the rings are shown in Fig. 2(f).

The transition to the spin-flop phase from the uniform ground state in bulk AFMs may occur either as the first-order phase transition with a jumplike change of magnetization along the external field direction or as two second-order transitions through the so-called canted phase. For a bulk AFM with a spatially homogeneous texture below and above the spin-flop transition, an appearance of the canted phase can be a consequence of the interplay between the exchange and single-ion anisotropy [2], higher-order anisotropy terms (e.g., cubic in addition to the uniaxial anisotropy) [9], or DMI [37–39]. In the case of ring-shaped AFM spin chains, the formation of the onion state is assured by the curvature-induced DMI with the energy density $\mathcal{E}_x^{\text{DMI}}$ and the Dzyaloshinskii vector $\mathbf{d} = 2\varkappa\mathbf{e}_B$. Being part of the expression for \mathcal{E}_x , the curvature-induced DMI allows rotation of \mathbf{n} in the ring plane; see orange line in Fig. 1(e) [23]. The canted state in AFM rings is observed for curvatures $\varkappa > \varkappa_{\text{cant}} \approx 0.585$, see yellow shaded region in Fig. 1(f) and details of the state compared with the onion in Figs. 3(a) and 3(b). We associate the appearance of the canted state with the competition between the Zeeman energy term \mathcal{E}_f , curvature-induced easy-axis anisotropy K^x , and DMI \mathcal{E}_{DM} . In this phase, the total magnetic moment of the ring in the field direction normalized by the number of magnetic sites, \mathcal{M} , grows with the external field faster than in the spin-flop phase, see Fig. 3(c) for magnetization and Fig. 3(d) for the differential susceptibility $\chi = \partial_h \mathcal{M}$. This is accompanied by a nonlinear decay of the total Néel vector \mathcal{N}_z measured along \mathbf{h} , see Fig. 3(e). The canted state is spatially inhomogeneous due to the competition between the spatially varying anisotropy axis \mathbf{e}_{ani} and homogeneous magnetic field \mathbf{h} , see schematics in Fig. 3(f)

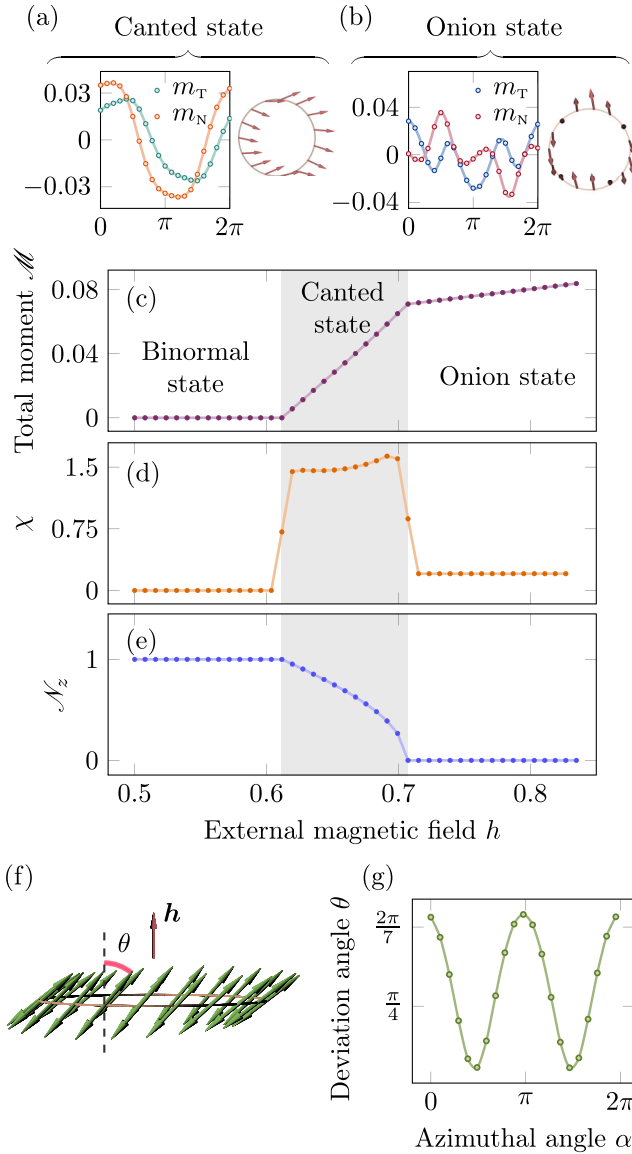


FIG. 3. Canted state in fields $\mathbf{h} \parallel \mathbf{e}_B$. (a) Components of the magnetization vector \mathbf{m} in the canted state for the ring with $\varkappa = 0.683$ exposed to the magnetic field $h = 0.66$. (b) Same for the onion state for the ring with $\varkappa = 0.683$, $h = 0.79$. The magnetic field dependence of (c) the equilibrium magnetic moment normalized by the number of magnetic sites, (d) the differential magnetic susceptibility, and (e) the total \mathbf{n} component along the field direction \mathcal{N}_z normalized by the number of magnetic sites. (f) Schematics of distribution of the Néel vector in the canted state. Dashed line coincides with the direction \mathbf{e}_B . The angle θ between $\mathbf{n}(\mathbf{r})$ and \mathbf{h} is indicated as well. Its spatial distribution is shown in panel (g). In all panels, symbols correspond to the results of simulations; lines are guides to the eye.

and the distribution of the angle between \mathbf{n} and \mathbf{h} , θ , along the azimuthal angle around the ring in Fig. 3(g).

Being exposed to the magnetic field of the order of the exchange field, $h \sim h^x = 1/\zeta$, spin chains experience the spin-flip phase transition after which the magnetic ordering becomes ferromagnetic; brown shaded region in Fig. 1(f). The Néel vector vanishes and the total magnetic moment of the

ring in the field direction reaches its saturation. Within the limit of the analytical model, which is linear with respect to ζ , the spin-flip field $h_{\text{spin-flip}} = h^x$. The critical transition fields, obtained from spin-lattice simulations (Appendix A), are reduced up to 0.4% of h^x , see the $h_{\text{spin-flip}}$ line in Fig 1(f). We associate this small deviation with effects in $\mathcal{O}(\zeta^2)$. The in-plane magnetization components, which emerged from \mathbf{n}' , produce local spatial modulation of the length of the magnetization vector in the onion state up to 12% in the vicinity of the spin-flop transition. The amplitude of this modulation decays with the increase of the field and is beyond the linear theory for the high-field states.

Approaching the spin-flip field, the critical curvature separating the spin-flop vortex and onion phases is reduced to $\varkappa_c^{\text{flip}} \approx 0.582$, see Fig 1(f). We attribute this change to the curvature-induced DMI, similarly to the appearance of the canted state near the vortex phase.

IV. REORIENTATION PHASE TRANSITIONS IN TILTED FIELDS

A finite external field applied under a certain angle to the ring axis, $\mathbf{h} = \hat{x}h_x + \hat{z}h_z$, breaks the rotational symmetry of the system, see Fig. 4(a). In uniaxial bulk AFMs (chiral and achiral), this can lead to the appearance of metastable states confined within the astroid-shaped region on the diagram of states in (h_x, h_z) coordinates [2,9,37]. In a curvilinear AFM, lowering of the system symmetry is accompanied by the lifting up of the translational symmetry of the system due to the spatial inhomogeneity of \mathbf{e}_{ani} . In the following, we discuss the field-induced states of a ring with curvature $\varkappa > \varkappa_c$ being in the onion state if $\mathbf{h} \parallel \mathbf{e}_B$. The field-induced transformation of the spin-flop vortex state with the field $\mathbf{h} = \hat{x}h_x + \hat{z}h_z$ is presented in Appendix C.

The (h_x, h_z) diagram of equilibrium states in the tilted magnetic field for the ring of curvature $\varkappa = 0.75$ is shown in Fig. 4(b). The equilibrium states and their stability regions are determined by analyzing the dependence of the differential susceptibility χ on h_z measured along the field direction for different h_x [Fig. 4(e)].

Even below the spin-flop transition, the tilted field develops a component of the total magnetic moment along \mathbf{h} supplemented by the spatially inhomogeneous texture for the Néel vector. At low h_z , the state which is referred to as the tilted one is developed from the binormal state and is similar to the state in the canted phase [cf. Figs. 3(f) and 4(a)]. Reflecting the symmetry of a ring, a representative distribution of the deviation angle of \mathbf{n} with α has two pronounced minima, see Fig. 4(c). The maximum deviation from the field axis θ_{max} is plotted as function of h_z for different h_x in Fig. 4(d). It depends on the relation between h_x and h_z . If $h_z \lesssim h_x$, keeping the ring in the tilted state, the deviation angle is close to $\pi/2$. The θ_{max} decreases with the increase of h_z and reaches a fixed value for the given h_x . In the tilted state, the total moment \mathcal{M} initially decreases because of the effective anisotropy along \mathbf{e}_B [Fig. 4(f)]. The respective regions of negative susceptibility are shown in Fig. 4(b) with light blue (decreasing negative χ with increasing h_z) and dark blue (increasing nonpositive χ with increasing h_z). The locus of fields corresponding to $\chi = 0$ is shown with open rhombuses.

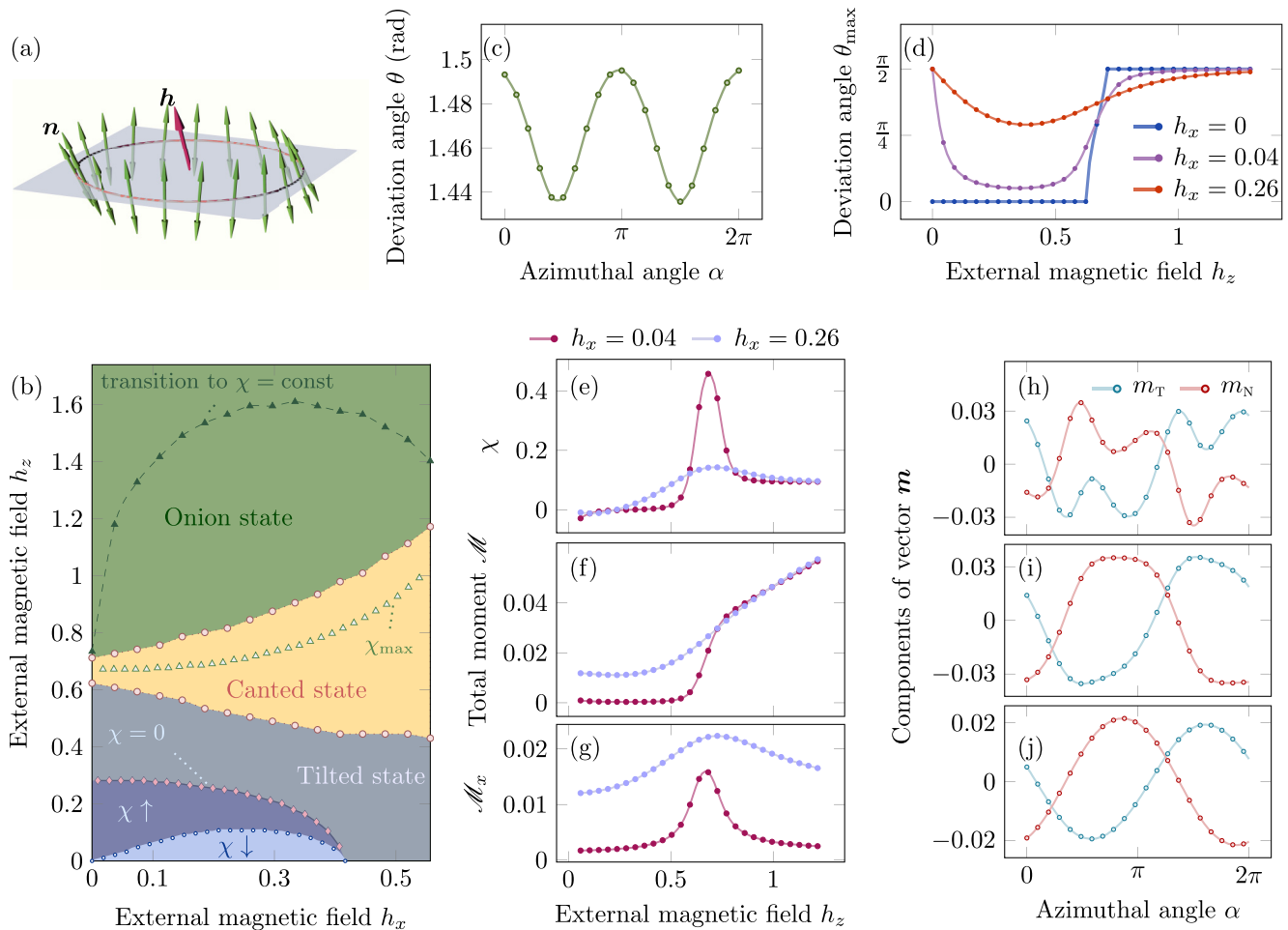


FIG. 4. AFM ring of curvature $\kappa = 0.75 > \kappa_c$ exposed to the magnetic field \mathbf{h} tilted from the easy axis. (a) Schematics of the distribution of the Néel vector in the tilted state. (b) The diagram of equilibrium states for different field directions. Simulations are performed with steps $\Delta h_x = 0.037$ and $\Delta h_z = 0.015$. (c) Spatial distribution of θ for $h_x = 0.04$ and $h_z = 0.83$. (d) Maximum angle θ_{\max} between the Néel vector and field direction as function of h_z for fixed h_x . (e) Differential susceptibility χ as function of the field component h_z shown for two different values of h_x . The magnetic field dependence of (f) the total magnetic moment normalized by the number of sites and (g) the magnetic moment along \hat{x} axis for the same values of h_x as used in panel (e). The change of the components of the magnetization vectors with the azimuthal angle α for the (h) onion, (i) canted, and (j) tilted states. In all panels, lines are guides to the eye and symbols correspond to simulation results. In panels (e)–(g), every third symbol from simulations is shown.

The region of the canted phase expands into regions of the tilted and onion states with larger h_x , see Fig. 4(b). The boundaries of the canted state in Fig. 4(b) are determined by the inflection points for the susceptibility $\chi(h_z)$. Proceeding to the canted state by the increase of h_z is characterized by the increase of θ_{\max} . The amplitude of the spatial distribution of the angle between \mathbf{n} and \mathbf{h} ($\theta_{\max} - \theta_{\min}$) reaches its maximum in the canted state (up to ≈ 0.2 rad for small h_x) and becomes smaller with θ_{\max} approaching $\pi/2$ in the onion state. Open triangles in Fig. 4(b) correspond to values of h_x and h_z at which the differential susceptibility χ reaches its maximum [Figs. 4(b) and 4(e)]. The tilted and canted states are similar with respect to the distribution of the magnetization vector, cf. Figs. 4(i) and 4(j). Still, we note that the mechanism of their stabilization reflected in the behavior of the magnetic susceptibility is different. The onion state in the tilted field is qualitatively similar to the one discussed for the field along \mathbf{e}_B , cf. Figs. 4(h) and 2(e).

The change of the total magnetic moment of the ring in a tilted field is shown in Figs. 4(f) and 4(g). There are three well-distinguished phases for sufficiently small h_x , namely, almost constant \mathcal{M} , rapidly growing \mathcal{M} , and slowly growing \mathcal{M} . The transition between phases becomes smoother with an increase of h_x . The component of the magnetic moment along the \hat{x} direction has a pronounced maximum within the canted state, see Fig. 4(g).

V. DISCUSSION

To summarize, we describe field-induced reorientation transitions of the Néel vector \mathbf{n} in an AFM spin chain consisting of an even number of spins arranged in a ring. The model accounts for the isotropic exchange, hard-axis anisotropy with the axis tangential to the ring and Zeeman interaction. Having intrinsic hard-axis anisotropy, such rings have a ground state with the Néel vector perpendicular to the ring's plane

independent of curvature in absence of external magnetic fields [23]. The critical fields, characteristic of the spin reorientation transitions, are determined by the curvature. The spin-flop state consists of vortex and onion phases for rings of small and large curvatures, respectively. The spin-flop transition behaves as the first-order one for rings with curvatures $\varkappa < \varkappa_{\text{cant}} \approx 0.585$. Otherwise, the transition is of the second order and happens via the intermediate canted state. The region of the canted state is expanded in fields applied under an angle to the ring axis. Approaching the spin-flip transition, the critical curvature between the vortex and onion states decreases to $\varkappa_c^{\text{flip}} \approx 0.582$. The onion state is characterized by a weak ferromagnetic response. The strength of the weak ferromagnetism is determined by n' . The respective moment lies in the plane of n' .

This paper provides insight into the influence of the geometric curvature on the spin reorientation transitions induced by external magnetic fields in curvilinear AFM spin chains. A spin chain arranged along plane curves is a paradigmatic example, which allows us to follow the phase transitions driven by the geometry for the case when the intrinsic anisotropy has its hard axis along the tangential direction. This hard axis anisotropy can be modified by or originate from the dipolar interaction [23]. Our results can be used to analyze the spin-flop transitions for other geometries and types of anisotropy, where the ground state is not necessarily uniform. We note that monitoring the curvature-dependent critical field, which is needed to induce the change of the magnetic state, provides a complementary method to determine material parameters for low-dimensional AFMs based on molecular magnets [40,41], DNA-based systems [42,43], or fabricated by means of atom-by-atom engineering [44,45].

The strength of the AFM exchange coupling in spin chains varies over several orders of magnitude, e.g., $\sim 10^{-24}$ J for Cu chains with monochloride bridges [46], $\sim 10^{-23}$ J for pyridine-based Cu chains [47], and $\sim 10^{-22}$ J for molecular wheels Cr_8Cd [48–50]. The latter is about an order of magnitude smaller than the exchange in the bulk Cr_2O_3 ($\sim 10^{-21}$ J) [51]. Assuming that a certain nanomagnet possesses the hard-axis intrinsic anisotropy with the strength of the same order as reported for Cr_8Cd [48,49], it is possible to estimate the magnetic length ℓ to be about 5 to 10 lattice constants and characteristic fields H_0 to be about 3.5 T, which is readily achievable in laboratory experiments. Such a molecular ring with eight atoms is expected to be in the spin-flop onion state. Parameters of the spin-flop transition can be also tuned in systems prepared by atom-by-atom engineered relying on the proper selection of the substrate and spin-carrying atoms [52]. Further experimental investigations of these systems and the comparison with the theoretical predictions of this paper should also give insight into the role of quantum effects in curvilinear low-dimensional AFMs. Lowering of the spin-flop and spin-flip fields in spin chains due to strong anisotropy, in comparison with bulk AFMs, paves the way toward reconfigurable spintronic devices, whose operational modes are different below and above the spin-flop transition.

The influence of the curvature-induced DMI on the spin-flop transition requires further analysis. In particular, it is insightful to compare the results presented above with the antiferromagnets in rolled-up geometries [53], which repre-

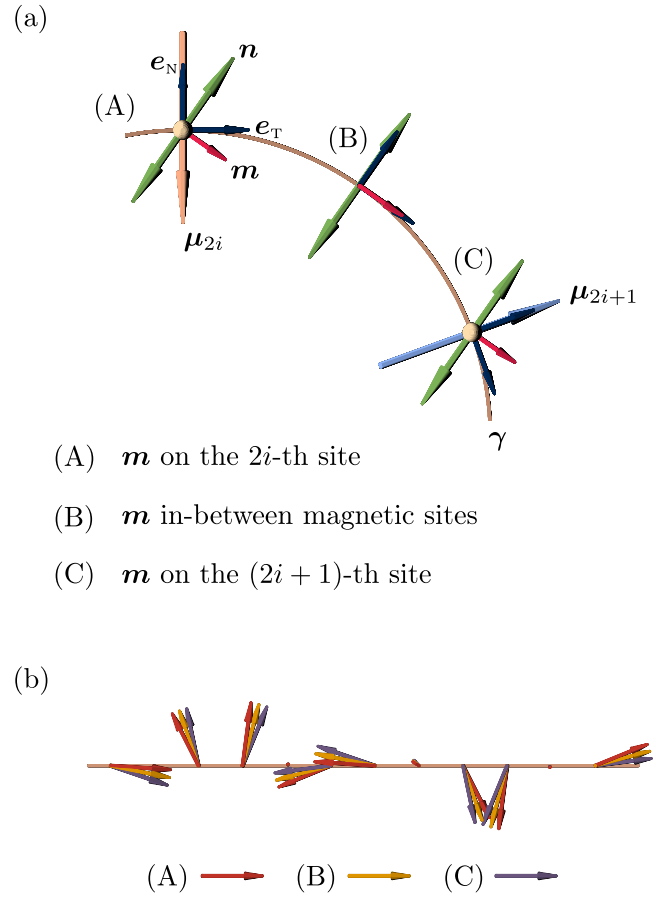


FIG. 5. Dependence of the weak ferromagnetic response on the spatial localization of the discrete order parameter along the curve γ . (a) i th AFM dimer consisting of μ_{2i} and μ_{2i+1} magnetic moments. Three possible orientations of n_i and m_i are shown for pairs of the order parameters at (A) $2i$ th site, (B) central point on the curve γ between the chain sites, and (C) $(2i+1)$ th site. (b) The change of the direction of the magnetization vectors for the ring with $\varkappa = 1.3$ exposed to the magnetic field $\mathbf{h} = 0.83\mathbf{e}_b$ in the onion state. In both panels, the lengths of the vectors are not to scale.

sent a development of the ring geometry into a tube. In planar chains, the presence of the Lifshitz invariant proportional to curvature is reflected in the appearance of the canted phase in external field for large ring curvatures. In contrast, AFM spin chains arranged along space curves have two Lifshitz invariants and possess the geometrically-governed helimagnetic phase transition driven by the Lifshitz invariant proportional to torsion in the absence of the field [23]. The presence of DMI terms of different symmetries in 3D curved spin chains should make the diagram of field-induced states richer. We anticipate that this behavior could be comparable with the spin-flop of a planar ring in the tilted field, since the homogeneous magnetic field does not coincide with the easy axis of a 3D spin chain.

ACKNOWLEDGMENTS

The authors thank Dr. Nina Elkina (HZDR) for support with simulations. Numerical calculations are performed using the OpenStack and Hemera facilities at the HZDR [54].

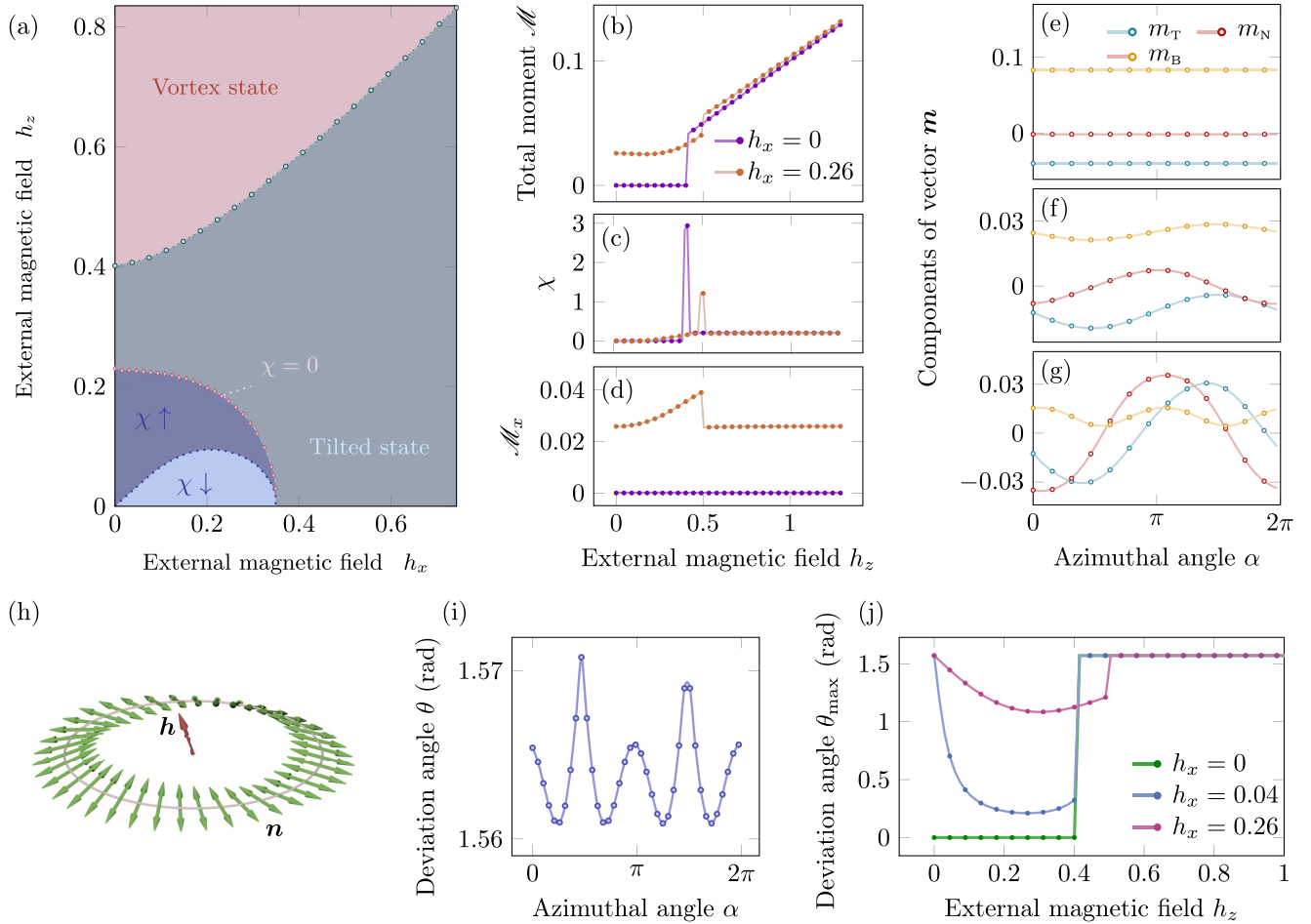


FIG. 6. Spin-flop vortex phase in the ring of curvature $\varkappa = 0.4 < \varkappa_{\text{cant}}$ exposed to a tilted external magnetic field. (a) The diagram of equilibrium states for different field directions. (b) The total magnetic moment normalized to the number of sites as function of the field h_z for two different values of h_x . The magnetic field dependence of (c) the differential susceptibility and (d) the magnetic moment along the \hat{x} axis for values of h_x as in (b). Components of the magnetization vectors for the (e) vortex state in $\mathbf{h} \parallel \mathbf{e}_B$, (f) vortex state in the tilted field, and (g) tilted states. (h) Schematics of the distribution of the Néel vector in the vortex state for $h_x = 0.78$ and $h_z = 1.75$. (i) The spatial distribution of the angle between the Néel vector and the field direction for $h_x = 0.26$ and $h_z = 0.83$. (j) Maximum angle between the Néel vector and the field direction as function of h_z for fixed h_x . In panels (b)–(g) and (j), every third symbol from simulations is shown.

Y.A.B. acknowledges financial support from the UKRATOP-project (funded by the BMBF; Reference No. 01DK18002). This work is financed in part via the German Research Foundation (DFG) under the Grants MC 9/22–1, MA 5144/22–1, MA 5144/24–1.

APPENDIX A: SPIN-LATTICE SIMULATIONS

To perform numerical analysis of curvilinear AFMs, we use the in-house developed SLaSi package [23,55]. The Landau–Lifshitz–Gilbert equation

$$\frac{d\boldsymbol{\mu}_i}{dt} = \frac{1}{\hbar S} \boldsymbol{\mu}_i \times \frac{\partial \mathcal{H}}{\partial \boldsymbol{\mu}_i} + \alpha_G \frac{d\boldsymbol{\mu}_i}{dt}, \quad i = \overline{1, N} \quad (\text{A1})$$

is solved numerically to obtain equilibrium magnetization states. Here, $\boldsymbol{\mu}_i$ is the unit vector of the magnetic moment for the i th chain site, \hbar is the reduced Planck's constant, α_G is the Gilbert damping, and N is the number of sites in the chain.

The spin-lattice Hamiltonian reads

$$\begin{aligned} \mathcal{H} = & \frac{\mathcal{J} S^2}{2} \left(\sum_{i=1}^{N-1} \boldsymbol{\mu}_i \cdot \boldsymbol{\mu}_{i+1} + \boldsymbol{\mu}_N \cdot \boldsymbol{\mu}_1 \right) \\ & + \frac{\mathcal{K} S^2}{2} \sum_{i=1}^N (\boldsymbol{\mu}_i \cdot \mathbf{e}_T^i)^2 - 2\mu_B S \sum_{i=1}^N \boldsymbol{\mu}_i \cdot \mathbf{H}. \end{aligned} \quad (\text{A2})$$

The length of all magnetic moments is the same, $|\boldsymbol{\mu}_i| = 1$, $i = \overline{1, N}$, and \mathbf{e}_T^i is the unit vector determining the tangential direction for the i th chain site. The sign of \mathcal{J} depends on the definition of the exchange part of the Hamiltonian. Here, $\mathcal{J} > 0$ favors the antiparallel orientation of $\boldsymbol{\mu}_i$, $\boldsymbol{\mu}_{i+1}$ in Eq. (A2). For all simulations, we used $\alpha_G = 0.5$, $S = 1$, $a_0 = 0.3$ nm, $\mathcal{J} = 1 \times 10^{-22}$ J, $\mathcal{K} = 4 \times 10^{-20}$ J, which gives $\ell = 5a_0$ and $\zeta = 0.1$. The system is considered to be in equilibrium if $\max |d\boldsymbol{\mu}_i/dt| < 10^{-14}$ Hz.

To determine the preferable equilibrium state for the given magnetic field, the relaxation is done for different initial states: With the Néel vector distribution being homogeneous

in the local or laboratory reference frames, namely, states $\mathbf{n} \parallel \mathbf{e}_B$, $\mathbf{n} \parallel \mathbf{e}_N$ and $\mathbf{n} \parallel \hat{x}$. After relaxation, their resulting distributions and energies are compared. The equilibrium state is considered to be the one possessing the lowest energy. To determine the boundary between the vortex and onion states, as well as boundaries between the states when the ring is exposed to a tilted magnetic field, additional simulations were done with the initial distribution set as in Eq. (5) for the given curvature. In the canted state region, every initial distribution relaxes to the canted state (vortex and onion states are not stable in this region). This is in contrast to the case of fields above the canted state, where the onion and vortex states can be metastable ones. The boundary of the region corresponding to the canted state in Fig. 1(f) is built based on the results of simulations with $\ell = 10a_0$ for $\mathcal{J} = 4 \times 10^{-22}$ J to provide a denser set of numerically obtained points.

APPENDIX B: DISCRETE ORDER PARAMETERS

In the continuum description, the Néel vector $\mathbf{n}(\mathbf{r})$ and magnetization vector $\mathbf{m}(\mathbf{r})$ are defined at each point \mathbf{r} of the curve. To compare respective micromagnetic models with spin lattice simulations, it is crucial to take into account that the i th AFM unit cell for spin chains is a dimer $\{\boldsymbol{\mu}_{2i}, \boldsymbol{\mu}_{2i+1}\}$. Furthermore, the anisotropy axis changes its direction for each of the magnetic moments within this dimer. The anisotropy direction per each magnetic moment is determined by the chain shape via its local atomistic surrounding and coordinates of the neighboring moments. Following the micromagnetic transition from the discrete to continuum models described in Ref. [28], in this paper, we associate the discrete order parameters

$\mathbf{n}_i = (\boldsymbol{\mu}_{2i} - \boldsymbol{\mu}_{2i+1})/(2\mu)$ and $\mathbf{m}_i = (\boldsymbol{\mu}_{2i} + \boldsymbol{\mu}_{2i+1})/(2\mu)$ with the spatial localization of the moment $\boldsymbol{\mu}_{2i}$. This is reflected in \mathcal{E}_{an} . One can rewrite the energy density of the intrinsic anisotropy as $\mathbf{n}\hat{K}\mathbf{n}$, where $\hat{K} = \begin{vmatrix} 1 & K^{\text{nd}}/2 & 0 \\ K^{\text{nd}}/2 & 0 & 0 \\ 0 & 0 & 0 \end{vmatrix}$ [28]. For the chosen location of the order parameters in the dimer, $K^{\text{nd}} = 2\zeta\kappa$. Other possibilities for a dimer placed on the curve $\boldsymbol{\gamma}$ are shown in Fig. 5. For a ring possessing a constant curvature, the point in the geometrical center of the dimer along $\boldsymbol{\gamma}$ has the tangential direction $\mathbf{e}_T^{2i+1/2}$ along the line connecting $2i$ th and $(2i+1)$ th sites ($K^{\text{nd}} = 0$). This is a special case of high symmetry specific for the ring geometry, which is absent for curves of arbitrary geometry.

APPENDIX C: SPIN FLOP VORTEX PHASE

The diagram of equilibrium states in a tilted field for the ring of curvature $\kappa < \kappa_{\text{cant}}$ possessing the spin-flop vortex state in $h_x = 0$ is shown in Fig. 6(a). An increase of the total magnetic moment with h reveals the first-order phase transition, see Fig. 6(b). The finite jumps in $\chi(h_z)$ in Fig. 6(c) are related to the discrete set of points to determine the phase transition by the difference scheme. A jump of the total magnetic moment along \hat{x} as a function of h_z being the consequence of the first-order transition is clearly seen in Fig. 6(d).

For nonzero h_x values, the tilted state is qualitatively similar to the tilted state discussed for $\kappa > \kappa_c$. The vortex state in the tilted field [Fig. 6(h)] is topologically equivalent to the spin-flop state in $\mathbf{h} \parallel \mathbf{e}_B$ [28] and exists for sufficiently large values of the field tilt angles. The deviation of the Néel vector from the symmetry plane measured by the angle θ as in Figs. 4(c) and 4(d) is shown in Figs. 6(i) and 6(j).

-
- [1] E. Turov, *Physical Properties of Magnetically Ordered Crystals* (Academic Press, New York, 1965).
- [2] B. A. Ivanov, Mesoscopic antiferromagnets: statics, dynamics, and quantum tunneling (Review), *Low Temp. Phys.* **31**, 635 (2005).
- [3] L. Šmejkal, A. H. MacDonald, J. Sinova, S. Nakatsuji, and T. Jungwirth, Anomalous Hall antiferromagnets, *Nat. Rev. Mater.* **7**, 482 (2022).
- [4] V. Baltz, A. Manchon, M. Tsoi, T. Moriyama, T. Ono, and Y. Tserkovnyak, Antiferromagnetic spintronics, *Rev. Mod. Phys.* **90**, 015005 (2018).
- [5] O. Gomonay, T. Jungwirth, and J. Sinova, Concepts of antiferromagnetic spintronics, *Phys. Status Solidi RRL* **11**, 1700022 (2017).
- [6] E. A. Turov, A. V. Kolchanov, V. V. Menshenin, I. F. Mirsayev, and V. V. Nikolaev, *Symmetry and Physical Properties of Antiferromagnets* (FIZMATLIT, Moscow, 2001).
- [7] A. M. Kosevich, B. A. Ivanov, and A. S. Kovalev, Magnetic solitons, *Phys. Rep.* **194**, 117 (1990).
- [8] A. B. Borisov and V. V. Kiselev, *Nonlinear Waves, Solitons and Localized Structures in Magnets*, in Russian (Russian Academy of Science, Yekaterinburg, 2011), Vol. 2.
- [9] A. N. Bogdanov, A. V. Zhuravlev, and U. K. Röbber, Spin-flop transition in uniaxial antiferromagnets: Magnetic phases, reorientation effects, and multidomain states, *Phys. Rev. B* **75**, 094425 (2007).
- [10] R. V. Pisarev, M. Fiebig, and D. Fröhlich, Nonlinear optical spectroscopy of magnetoelectric and piezomagnetic crystals, *Ferroelectrics* **204**, 1 (1997).
- [11] M. S. Wörnle, P. Welter, M. Giraldo, T. Lottermoser, M. Fiebig, P. Gambardella, and C. L. Degen, Coexistence of Bloch and Néel walls in a collinear antiferromagnet, *Phys. Rev. B* **103**, 094426 (2021).
- [12] O. Gomonay, V. Baltz, A. Brataas, and Y. Tserkovnyak, Antiferromagnetic spin textures and dynamics, *Nat. Phys.* **14**, 213 (2018).
- [13] Y. Oh, S. Artyukhin, J. Yang, V. Zapf, J. W. Kim, D. Vanderbilt, and S.-W. Cheong, Non-hysteretic colossal magnetoelectricity in a collinear antiferromagnet, *Nat. Commun.* **5**, 3201 (2014).
- [14] R. Lebrun, A. Ross, S. A. Bender, A. Qaiumzadeh, L. Baldrati, J. Cramer, A. Brataas, R. A. Duine, and M. Kläui, Tunable long-distance spin transport in a crystalline antiferromagnetic iron oxide, *Nature (London)* **561**, 222 (2018).
- [15] P. F. Bessarab, D. Yudin, D. R. Gulevich, P. Wadley, M. Titov, and O. A. Tretiakov, Stability and lifetime of antiferromagnetic skyrmions, *Phys. Rev. B* **99**, 140411(R) (2019).
- [16] S. K. Upadhyay and E. V. Sampathkumaran, Multiferroicity in a spin-chain compound, $\text{Tb}_2\text{BaCoO}_5$, with exceptionally large

- magnetodielectric coupling in polycrystalline form, *Appl. Phys. Lett.* **112**, 262902 (2018).
- [17] D. Peters, I. P. McCulloch, and W. Selke, Quantum Heisenberg antiferromagnetic chains with exchange and single-ion anisotropies, *J. Phys.: Conf. Ser.* **200**, 022046 (2010).
- [18] O. Prokhnenko, G. Marmorini, S. E. Nikitin, D. Yamamoto, A. Gazizulina, M. Bartkowiak, A. N. Ponomaryov, S. A. Zvyagin, H. Nojiri, I. F. Díaz-Ortega, L. M. Anovitz, A. I. Kolesnikov, and A. Podlesnyak, High-field spin-flop state in green diopside, *Phys. Rev. B* **103**, 014427 (2021).
- [19] P. Fischer, D. Sanz-Hernández, R. Streubel, and A. Fernández-Pacheco, Launching a new dimension with 3D magnetic nanostructures, *APL Mater.* **8**, 010701 (2020).
- [20] D. D. Sheka, A perspective on curvilinear magnetism, *Appl. Phys. Lett.* **118**, 230502 (2021).
- [21] R. Streubel, E. Y. Tsymbal, and P. Fischer, Magnetism in curved geometries, *J. Appl. Phys.* **129**, 210902 (2021).
- [22] D. Makarov, O. M. Volkov, A. Kákay, O. V. Pylypovskiy, B. Budinská, and O. V. Dobrovolskiy, New dimension in magnetism and superconductivity: 3D and curvilinear nanoarchitectures, *Adv. Mater.* **34**, 2101758 (2022).
- [23] O. V. Pylypovskiy, D. Y. Kononenko, K. V. Yershov, U. K. Röbber, A. V. Tomilo, J. Fassbender, J. van den Brink, D. Makarov, and D. D. Sheka, Curvilinear one-dimensional antiferromagnets, *Nano Lett.* **20**, 8157 (2020).
- [24] H. Wu and J. Lan, Curvilinear manipulation of polarized spin waves, *Phys. Rev. B* **105**, 174427 (2022).
- [25] S. Castillo-Sepúlveda, R. A. Escobar, D. Altbir, M. Krizanac, and E. Y. Vedmedenko, Magnetic Möbius stripe without frustration: Noncollinear metastable states, *Phys. Rev. B* **96**, 024426 (2017).
- [26] K. V. Yershov, Dynamics of domain walls in curved antiferromagnetic wires, *Phys. Rev. B* **105**, 064407 (2022).
- [27] K. V. Yershov, A. Kákay, and V. P. Kravchuk, Curvature-induced drift and deformation of magnetic skyrmions: Comparison of the ferromagnetic and antiferromagnetic cases, *Phys. Rev. B* **105**, 054425 (2022).
- [28] O. V. Pylypovskiy, Y. A. Borysenko, J. Fassbender, D. D. Sheka, and D. Makarov, Curvature-driven homogeneous Dzyaloshinskii–Moriya interaction and emergent weak ferromagnetism in anisotropic antiferromagnetic spin chains, *Appl. Phys. Lett.* **118**, 182405 (2021).
- [29] N. Papanicolaou and W. J. Zakrzewski, Dynamics of interacting magnetic vortices in a model Landau–Lifshitz equation, *Physica D* **80**, 225 (1995).
- [30] For a generic uniaxial antiferromagnet, a small magnetization appearing in the spin-flop phase is determined by the relation between constants of anisotropy and uniform exchange in a continuum description, which is usually much smaller than the saturation magnetization ($m \ll n$ in dimensionless units) [2,9]. For spin chains considered in this paper, the magnitude of m at spin-flop fields can be estimated from Eq. (2) with $\zeta = 0.1$ and $\max h_{sf} \lesssim 0.8$ as $\max m \lesssim 0.08 \ll 1$.
- [31] *NIST Handbook of Mathematical Functions*, edited by F. W. J. Olver, D. W. Lozier, R. F. Boisvert, and C. W. Clark (Cambridge University Press, New York, 2010).
- [32] J. Rothman, M. Kläui, L. Lopez-Diaz, C. A. F. Vaz, A. Bleloch, J. A. C. Bland, Z. Cui, and R. Speaks, Observation of a Bi-Domain State and Nucleation Free Switching in Mesoscopic Ring Magnets, *Phys. Rev. Lett.* **86**, 1098 (2001).
- [33] A. Kosiorek, W. Kandulski, H. Glacynska, and M. Giersig, Fabrication of nanoscale rings, dots, and rods by combining shadow nanosphere lithography and annealed polystyrene nanosphere masks, *Small* **1**, 439 (2005).
- [34] D. D. Sheka, V. P. Kravchuk, and Y. Gaididei, Curvature effects in statics and dynamics of low dimensional magnets, *J. Phys. A: Math. Theor.* **48**, 125202 (2015).
- [35] D. Kong, S. Wang, and C. Chen, Magnetization ground states and phase diagrams for a nanosized Co hollow sphere: An onion-type magnetization state, *J. Appl. Phys.* **104**, 013923 (2008).
- [36] V. P. Kravchuk, U. K. Röbber, O. M. Volkov, D. D. Sheka, J. van den Brink, D. Makarov, H. Fuchs, H. Fangohr, and Y. Gaididei, Topologically stable magnetization states on a spherical shell: Curvature-stabilized skyrmions, *Phys. Rev. B* **94**, 144402 (2016).
- [37] O. G. Medvedovskaya and G. K. Chepurnykh, Dzyaloshinskii interaction effect on orientational phase-transitions in antiferromagnets, *Solid State Phys.* **27**, 718 (1985).
- [38] T. Thio, C. Y. Chen, B. S. Freer, D. R. Gabbe, H. P. Janssen, M. A. Kastner, P. J. Picone, N. W. Preyer, and R. J. Birgeneau, Magnetoresistance and the spin-flop transition in single-crystal $\text{La}_2\text{CuO}_{4+y}$, *Phys. Rev. B* **41**, 231 (1990).
- [39] I. Tsukada, J. Takeya, T. Masuda, and K. Uchinokura, Two-Stage Spin-Flop Transitions in the Antiferromagnetic Spin Chain $\text{BaCu}_2\text{Si}_2\text{O}_7$, *Phys. Rev. Lett.* **87**, 127203 (2001).
- [40] M. G. Sorolla, X. Wang, T. Makarenko, and A. J. Jacobson, A large spin, magnetically anisotropic, octanuclear vanadium(III) wheel, *Chem. Commun.* **55**, 342 (2019).
- [41] X.-X. Fu, F. Wei, Y. Niu, and C.-K. Wang, Designing high-performance spin filters and valves based on metal-salphen molecular chains, *Phys. E* **131**, 114737 (2021).
- [42] K. Mizoguchi, S. Tanaka, M. Ojima, S. Sano, M. Nagatori, H. Sakamoto, Y. Yonezawa, Y. Aoki, H. Sato, K. Furukawa, and T. Nakamura, AF-like ground state of Mn-DNA and charge transfer from Fe to base- π -band in Fe-DNA, *J. Phys. Soc. Jpn.* **76**, 043801 (2007).
- [43] M. R. Kesama, B. K. Yun, S. R. Dugasani, J. H. Jung, and S. H. Park, Enhancing the electrical, optical, and magnetic characteristics of DNA thin films through Mn^{2+} fortification, *Colloids Surf. B* **167**, 197 (2018).
- [44] S. Loth, S. Baumann, C. P. Lutz, D. M. Eigler, and A. J. Heinrich, Bistability in atomic-scale antiferromagnets, *Science* **335**, 196 (2012).
- [45] A. A. Khajetoorians, J. Wiebe, B. Chilian, S. Lounis, S. Blügel, and R. Wiesendanger, Atom-by-atom engineering and magnetometry of tailored nanomagnets, *Nat. Phys.* **8**, 497 (2012).
- [46] R. C. Santana, B. N. Ferreira, J. R. Sabino, J. F. Carvalho, O. Peña, and R. Calvo, Structure and magnetism of catena-poly[copper(II)- μ -dichloro-L-lysine]hemihydrate: Copper chains with monochloride bridges, *Polyhedron* **47**, 53 (2012).
- [47] B. Drahoš, R. Herchel, and Z. Trávníček, Structural, magnetic, and redox diversity of first-row transition metal complexes of a pyridine-based macrocycle: Well-marked trends supported by theoretical dft calculations, *Inorg. Chem.* **54**, 3352 (2015).
- [48] Y. Furukawa, K. Kiuchi, K.-i. Kumagai, Y. Ajiro, Y. Narumi, M. Iwaki, K. Kindo, A. Bianchi, S. Carretta, G. A. Timco, and R. E. P. Winpenny, Topological effects on the magnetic properties of closed and open ring-shaped Cr-based antiferromagnetic nanomagnets, *Phys. Rev. B* **78**, 092402 (2008).

- [49] T. Guidi, B. Gillon, S. A. Mason, E. Garlatti, S. Carretta, P. Santini, A. Stunault, R. Caciuffo, J. van Slageren, B. Klemke, A. Cousson, G. A. Timco, and R. E. P. Winpenny, Direct observation of finite size effects in chains of antiferromagnetically coupled spins, *Nat. Commun.* **6**, 7061 (2015).
- [50] E. Garlatti, G. Allodi, S. Bordignon, L. Bordonali, G. A. Timco, R. E. P. Winpenny, A. Lascialfari, R. D. Renzi, and S. Carretta, Breaking the ring: ^{53}Cr -NMR on the Cr_8Cd molecular nanomagnet, *J. Phys.: Condens. Matter* **32**, 244003 (2020).
- [51] Y. Kota and H. Imamura, Narrowing of antiferromagnetic domain wall in corundum-type Cr_2O_3 by lattice strain, *Appl. Phys. Express* **10**, 013002 (2017).
- [52] C. F. Hirjibehedin, C.-Y. Lin, A. F. Otte, M. Ternes, C. P. Lutz, B. A. Jones, and A. J. Heinrich, Large magnetic anisotropy of a single atomic spin embedded in a surface molecular network, *Science* **317**, 1199 (2007).
- [53] T. Ueltzhöffer, R. Streubel, I. Koch, D. Holzinger, D. Makarov, O. G. Schmidt, and A. Ehresmann, Magnetically patterned rolled-up exchange bias tubes: A pater-noster for superparamagnetic beads, *ACS Nano* **10**, 8491 (2016).
- [54] High Performance Computing at Helmholtz-Zentrum Dresden-Rossendorf.
- [55] SLaSi spin-lattice simulations package.